Materials Horizons

ROYAL SOCIETY OF CHEMISTRY

COMMUNICATION

View Article Online
View Journal | View Issue

Cite this: *Mater. Horiz.*, 2025, 12, 4349

Received 25th December 2024,
Accepted 13th March 2025

DOI: 10.1039/d4mh01897d

rsc.li/materials-horizons

Scalable assembly of micron boron nitride into high-temperature-resistant insulating papers with superior thermal conductivity†

Meng-Xin Liu,[a] Rui-Yu Ma,[a] Zhi-Xing Wang,[b] Zhuo-Yang Li,[c] Gui-Lin Song,[a] Jie Lin,[a] Xin-Yuan Li,[a] Ling Xu,*[c] Ding-Xiang Yan,[c] Li-Chuan Jia*[b] and Zhong-Ming Li[a]

With the rapid development of modern electrical equipment towards miniaturization, integration, and high power, high-temperature-resistant insulating papers with superior thermal conductivity are highly desirable for ensuring the reliability of high-end electrical equipment. However, it remains a challenge for current insulating papers to achieve this goal. Herein, we demonstrate the design of high-temperature-resistant micron boron nitride (m-BN) based insulating papers with superior thermal conductivity by a universal and scalable one-step assembly strategy. Inspired by the floating shape of jellyfish in the ocean, aramid nanofibers (ANF) resembling the tentacles of jellyfish were employed to support the bell-shaped m-BN, which effectively addresses the kinetically stable dispersion and film-forming ability of m-BN. The resultant m-BN@ANF papers exhibit excellent high-temperature-resistant insulating performance with an ultra-high breakdown strength of 359.0 kV mm^{-1} even at a high temperature of 200 °C, far exceeding those of these previously reported systems. In addition, the optimal m-BN@ANF paper demonstrates a superior thermal conductivity of 26.4 W m^{-1} K^{-1} and an excellent thermostability with an initial decomposition temperature of 486 °C. This outstanding comprehensive performance demonstrates the promise of applying these m-BN@ANF papers in advanced electrical systems operating under high-temperature circumstances.

New concepts

The serious degradation of electrical insulation properties at high temperatures is one of the most important challenges for the application of current insulating papers in electrical equipment. In this work, we propose an innovative approach to fabricate high-temperature resistant insulating papers with superior thermal conductivity. Inspired by the floating shape of jellyfish in the ocean, aramid nanofibers (ANF) act as the tentacles of jellyfish to address the kinetically stable dispersion and film-formation problems of micron boron nitride (m-BN). The large size of m-BN effectively blocks the development of electric trees and facilitates phonon transport. Thus, the resultant m-BN@ANF papers achieve an ultra-high breakdown strength of 359.0 kV mm^{-1} even at a high temperature of 200 °C, which far exceeds the values reported in previous works. Meanwhile, the m-BN@ANF papers also have a superior thermal conductivity of 26.4 W m^{-1} K^{-1} and excellent thermostability with an initial decomposition temperature of 486 °C. This strategy realizes the optimization of the electrical insulation properties, thermal conductivity and thermostability of insulating papers, simultaneously, which provides a promising idea in the direction of high-temperature-resistant insulating papers.

Introduction

With the rapid development of electrical power, rail transit, aerospace, and other fields, advanced insulating materials are urgently required for manufacturing high-end electrical equipment.[1–4] In addition to good electrical insulation properties, ideal insulating materials must also possess high thermostability, superior thermal conductivity (TC), and good mechanical flexibility to adapt to extreme working environments (*e.g.* large instantaneous power, high voltage, and elevated temperature).[5–7] Ceramics and polymers are two important insulating materials and have been widely used in various electrical and electronic systems.[8–11] Nevertheless, the production of advanced insulating papers using ceramics and polymers separately remains challenging owing to their inherent limitations, such as brittleness and the poor film-forming ability of ceramics, and a low TC and poor thermostability of polymers.

Recently, the assembly of 2D ceramic nanosheets (*e.g.* mica nanosheets, montmorillonite nanosheets, and boron nitride nanosheets (BNNS)) with polymer matrices to produce

[a] College of Polymer Science and Engineering, State Key Laboratory of Polymer Materials Engineering, Sichuan University, Chengdu, 610065, China
[b] College of Electrical Engineering, Sichuan University, Chengdu, 610065, China. E-mail: lcjia@scu.edu.cn
[c] School of Aeronautics and Astronautics, Sichuan University, Chengdu, 610065, China. E-mail: lingxu@scu.edu.cn

† Electronic supplementary information (ESI) available. See DOI: https://doi.org/10.1039/d4mh01897d

nacre-like ceramic/polymer papers has emerged as a promising approach for manufacturing advanced insulating materials.[12–15] Among these ceramic nanosheets, BNNS have attracted tremendous attention due to their high dielectric breakdown strength (E_b) (~700 kV mm^{-1}) and high TC (~400 W m^{-1} K^{-1}).[16,17] It is reported that the incorporation of BNNS into polymer matrices could endow the composites with highly insulating and thermal conductive performances, such as 39.8 kV mm^{-1}@1.16 W m^{-1} K^{-1} for the BNNS/polydimethylsiloxane composites,[18] 134.7 kV mm^{-1}@5.59 W m^{-1} K^{-1} for the BNNS/polyvinyl alcohol composites,[19] and 148.6 kV mm^{-1}@9.25 W m^{-1} K^{-1} for the BNNS/polyurethane composites.[20] However, the used polymer matrices for these composite papers tend to exhibit weak heat resistance characteristics, limiting their application under high-temperature circumstances. To date, various thermostable polymers have been exploited to manufacture high-temperature-resistant insulating papers, including aramid nanofibers (ANF), poly-*p*-phenylene benzoxazole fibers (PBO), polyimide (PI), *etc.* For example, Teng *et al.* reported the fabrication of highly thermostable BNNS/ANF/aramid pulp composites, which showed a good E_b of 59.6 kV mm^{-1} and an in-plane TC of 4.34 W m^{-1} K^{-1} at 20 wt% BNNS content.[21] A much higher E_b and in-plane TC (238.7 kV mm^{-1}@7.75 W m^{-1} K^{-1}) are achieved in the BNNS/ANF composites at a higher BNNS content (40 wt%).[22] Although considerable progress has been made, there are still some longstanding bottlenecks for the fabrication of high-performance BNNS/polymer papers: (1) abundant interfaces are induced between adjacent BNNS due to their nanoscale effects, resulting in the modest enhancement efficiency in E_b and TC; (2) the scalable exfoliation technique to yield BNNS dispersion has not yet been realized, rendering it difficult to apply BNNS dispersion on a large scale; (3) it is crucial to guarantee stability for the insulating papers under high temperature circumstances, which is absent for the BNNS/polymer papers previously reported. Consequently, there is an urgent requirement to develop an efficient and scalable strategy for fabricating high-temperature-resistant insulating papers.

In contrast to BNNS, micron-BN sheets (m-BN) with high crystallinity are promising candidates to realize the facile and scalable fabrication of high-temperature-resistant insulating materials, in view of easy industrialization, and low cost.[6,23–27] More importantly, the large size feature of m-BN is expected to provide a larger contact area between the adjacent m-BN and thus reduce the number of interface boundaries and defects, as compared to the BNNS in the composites.[27] This not only contributes to blocking the development of electric trees more effectively, but also facilitates phonon transport, thereby enhancing the E_b and TC of the insulating papers. However, the high crystallinity and large size characteristics of m-BN are a double-edged sword, which makes it daunting and challenging to yield a kinetically stable m-BN dispersion and thus realize the assembly of m-BN with thermostable polymers into high-temperature-resistant insulating papers.[28–30]

Herein, inspired by the floating shape of jellyfish in the ocean, we report a universal and scalable one-step assembly strategy to realize kinetically stable dispersion and film-forming ability of m-BN by coupling it with fibrous ANF. In such a structure, the ANF resemble the tentacles of a jellyfish to support the bell-shaped m-BN, endowing the m-BN@ANF ink with a favorable kinetic dispersibility (Fig. 1a). The resultant m-BN@ANF ink has been proven to be able to efficiently prepare

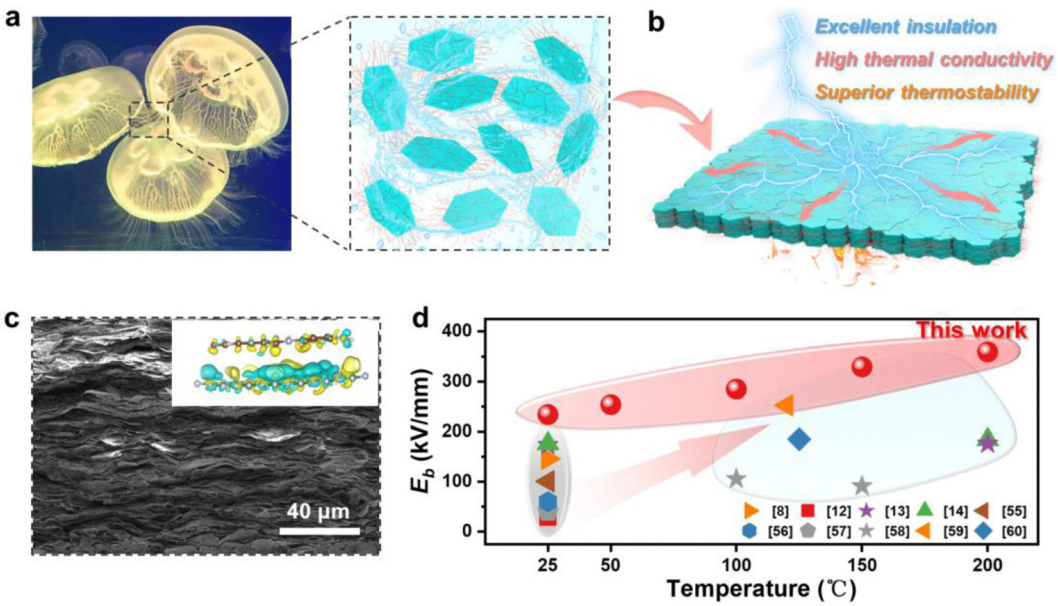

Fig. 1 Design concept for the m-BN@ANF papers. (a) Schematic of the m-BN@ANF ink dispersion form inspired by the floating jellyfish structure. (b) Schematic structure of m-BN@ANF insulating papers. (c) SEM images of the m-BN@ANF papers and the embedded plot show the charge density difference of m-BN@ANF. (d) Comparison of the breakdown strength of m-BN@ANF papers with previously reported insulating papers at different temperatures.

high-temperature-resistant insulating papers through various film-forming methods (Fig. 1b and c). Our assembly strategy gives the m-BN@ANF papers competitive advantages over those prepared using the traditional assembly strategy: (1) achieving an ultra-high E_b value of 359.0 kV mm^{-1} even at a high temperature of 200 °C, far exceeding that of those previously reported systems (Fig. 1d); (2) realizing a superior TC value of 26.4 W m^{-1} K^{-1}, excellent thermostability with an initial decomposition temperature of 486 °C, and outstanding flame retardancy with a VTM-0 rating, ensuring reliability in extreme environments; (3) possessing excellent film-forming ability and good universality to the film-forming methods, including blade coating, casting, and vacuum filtration. These good comprehensive properties of the m-BN@ANF papers, combined with the facile and scalable manufacturing strategy, make them ideal candidates for high-temperature insulation applications.

Results and discussion

Preparation and characterization of the m-BN@ANF ink

Realizing the kinetically stable dispersion of m-BN is a prerequisite for the fabrication of high-performance m-BN based papers. ANF is employed as a building block to address the dispersion problem of m-BN, due to its abundant π–π conjugated structures, good dispersibility and high specific surface area.[23,31] Fig. 2a schematically shows the preparation process of the stable m-BN@ANF ink. First, the alkaline dissolution method (DMSO/KOH/H_2O) was adopted to yield a stable ANF dispersion by enabling the deprotonation of the

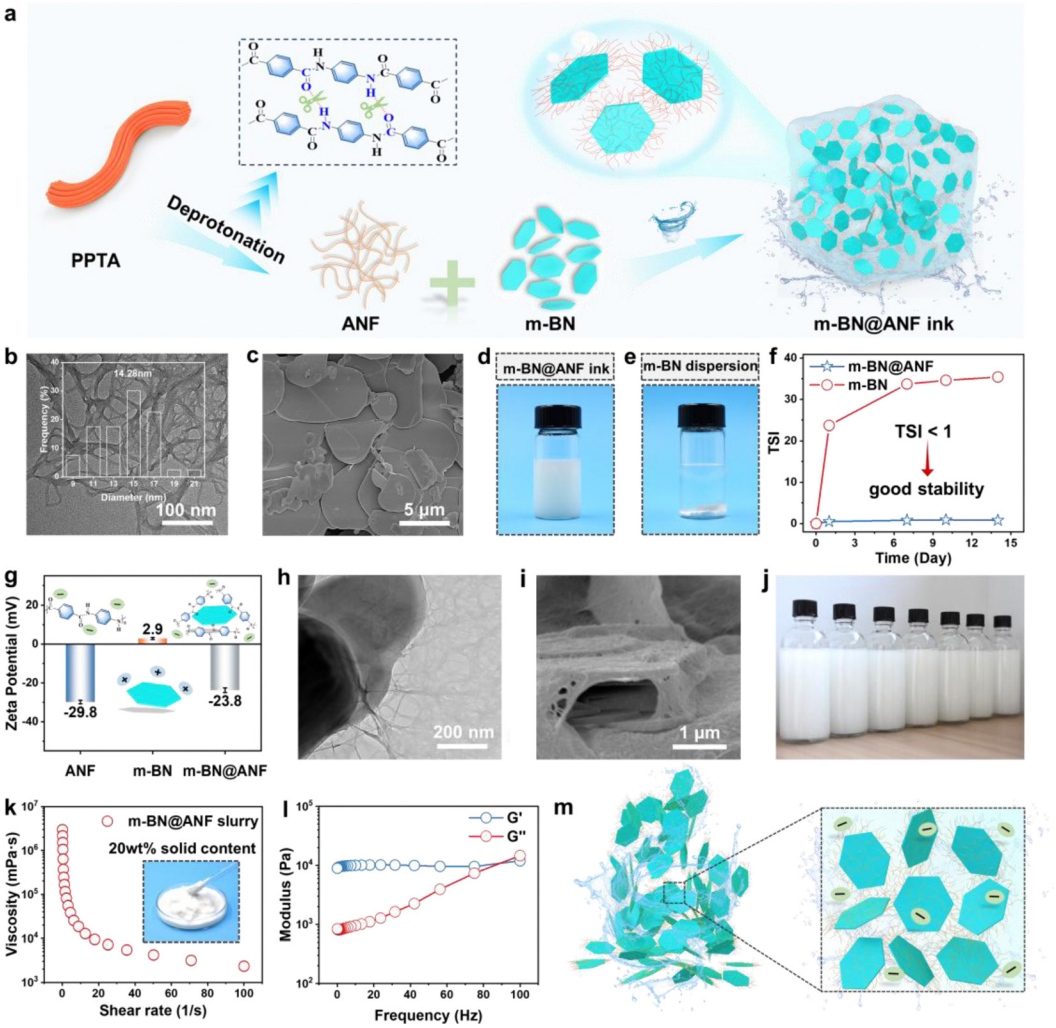

Fig. 2 Preparation and characterization of the m-BN@ANF ink. (a) Schematic illustration of the fabrication process of the m-BN@ANF ink. (b) TEM image of the ANF. (c) SEM image of m-BN. Digital photographs of (d) the m-BN@ANF ink and (e) the m-BN dispersion. (f) TSI values of the m-BN@ANF ink and the m-BN dispersion. (g) Zeta potentials of the ANF dispersion, the m-BN dispersion, and the m-BN@ANF ink. (h) TEM image and (i) SEM image of the m-BN@ANF ink. (j) Digital photograph showing large quantities of the stable m-BN@ANF inks. (k) Steady shear viscosity of the m-BN@ANF slurry. The inset image shows a digital photograph of the m-BN@ANF slurry. (l) Shear modulus of the m-BN@ANF slurry. (m) Schematic diagram of the dispersed form between m-BN and ANF in the m-BN@ANF ink.

poly-*p*-phenylene terephthalamide (PPTA) molecular chains (Fig. S1, ESI†). The transmission electron microscopy (TEM) image in Fig. 2b reveals that the synthesized ANFs exhibit a nanoscale fiber morphology, with an average fiber diameter of approximately 15 nm. Then, m-BN with an average lateral size of approximately 10 μm was added to the ANF dispersion to obtain a stable m-BN@ANF ink *via* facile mechanical stirring (Fig. 2c, d and Fig. S2, ESI†). It is clearly observed that the m-BN@ANF ink (the weight ratio of m-BN to ANF is 9 : 1) exhibits excellent kinetic stability, without any obvious settlement, even after static storage for 30 days, in sharp contrast to the non-dispersibility of the m-BN (Fig. 2e and Fig. S3, ESI†). Multiple light scattering experiments were subsequently employed to quantitatively evaluate the stability of the m-BN@ANF ink. More specifically, after standing for 14 days, the Turbiscan Stability Index (TSI) value of the m-BN@ANF ink is only 0.9, while that of the m-BN dispersion reaches 35.0, confirming the excellent stability of the m-BN@ANF ink (Fig. 2f). Additionally, the zeta potential value is only 2.9 mV for the m-BN dispersion, while a value of −23.8 mV was obtained for the m-BN@ANF ink. This result implies the presence of strong electrostatic repulsion in the m-BN@ANF ink, which contributes to preventing m-BN aggregation (Fig. 2g).[32] These results demonstrate that only a tiny amount of ANF was able to achieve good dispersion of m-BN in water. TEM and scanning electron microscopy (SEM) were later employed to investigate the overlapping morphology between the m-BN and ANF (Fig. 2h, i and Fig. S4, ESI†). It is clearly observed that m-BN@ANF exhibits a jellyfish-like structure, in which m-BN serves as the bell-shaped body of the jellyfish, and one end of numberless ANF tightly adheres to the surface of m-BN, while the other end hangs off the edges of m-BN, acting as the tentacles of the jellyfish and providing stable support for the m-BN bell-shaped body in water.[33] Surprisingly, owing to the easily scalable preparation process, large quantities of stable m-BN@ANF inks could be easily manufactured (Fig. 2j and Fig. S5, ESI†). Moreover, the m-BN@ANF slurry suitable for blade coating can also be readily produced (Fig. 2k). Rheological experiments show that the storage modulus (G') is higher than the loss modulus (G'') of the m-BN@ANF slurry in the low-frequency region, proving the good kinetic dispersion stability of the slurry (Fig. 2l). Based on the above results, it can be inferred from the schematic diagram of the dispersed form of m-BN and ANF (Fig. 2m), the existence of strong interfacial interactions between m-BN and ANF.

The stabilization mechanism of the m-BN@ANF ink

To elucidate the mechanism of kinetically stable dispersion of the m-BN@ANF ink, density functional theory (DFT) calculations are employed to investigate the interfacial interaction between m-BN and ANF at the molecular level (Fig. S6, ESI†). As shown in Fig. 3a, the electronic thresholding function (ELF) shows a significant charge transfer between m-BN and ANF. Specifically, in Fig. 3b, the blue areas represent lost electrons, and the red areas represent gained electrons, so it is clear that the charge is transferred from ANF to m-BN, and the Bader charge value is calculated to be 2.445 *e*, indicating a possible interaction between m-BN and ANF.[34,35] In addition, adsorption energy describes the decrease in energy when two materials combine during adsorption, it can be used to characterize the difficulty level of synthesizing compounds from different components.[36] When the adsorption energy is negative, it represents the presence of interaction between the components, and if it is positive, it is not easy to form interaction.[37] Based on the m-BN@ANF mixture model, the adsorption energy of the mixture was calculated as follows:

$$E_{ads} = E_{m\text{-}BN@ANF} - E_{m\text{-}BN} - E_{ANF} \quad (1)$$

where $E_{m\text{-}BN@ANF}$ represents the total energy of the m-BN@ANF mixture after adsorption, while $E_{m\text{-}BN}$ and E_{ANF} represent the total energies of the isolated m-BN and ANF molecules, respectively (more details are described in the ESI†).[38–40]

The formation energy of the m-BN@ANF mixture is calculated as −1.171 eV, indicating the presence of non-negligible interaction between m-BN and ANF (Table S1, ESI†). Reduced density gradient (RDG) analysis was performed on the mixture to further determine the specific interaction between m-BN and ANF.[41] The obtained results in Fig. 3c indicate the existence of van der Waals forces between m-BN and ANF, which can be attributed to π–π interactions between m-BN and ANF.

Furthermore, molecular dynamics (MD) simulation was conducted to analyze the assembly process of m-BN and ANF in water (Fig. S7, ESI†).[42,43] Initially, m-BN and ANF were randomly distributed in water, and subsequently, the two components gradually approach each other. Eventually, the ANF adheres tightly to the m-BN surface, and a stable m-BN@ANF mixture is generated (Fig. 3d). In sharp contrast, the obvious m-BN aggregation was observed for the m-BN dispersion in a relatively short period of time (Fig. 3e). These phenomena indicate that the strong π–π interaction between m-BN and ANF plays a crucial role in the stable dispersion of the ink (Fig. S8, ESI†).[44] To further demonstrate the successful adhesion of ANF to the m-BN surface, the radial distribution function (RDF) of the ANF around a specified m-BN was calculated.[45] Fig. 3f clearly reflects that the ANF tends to approach the m-BN surface, therefore, as m-BN and ANF gradually approach each other, the van der Waals forces between them gradually increases (Fig. 3g). Compared with the m-BN dispersion, the van der Waals forces between the m-BNs in the m-BN@ANF ink system is reduced, confirming that the generation of van der Waals forces between the ANF and m-BN effectively inhibits m-BN agglomeration, thereby promoting stable dispersion of the m-BN@ANF ink (Fig. S9, ESI†). In addition, ultraviolet-visible (UV-vis) spectra were also used to analyze the interfacial interaction between m-BN and ANF in the m-BN@ANF ink, and the results are shown in Fig. 3h. The spectrum of ANF exhibits a broad absorption peak at 336 nm, and when it forms a composite with m-BN, the spectrum of the m-BN@ANF ink show a broad absorption peak at 338 nm. The peak of the m-BN@ANF shifted to a higher field by 2 nm compared to ANF, which also proves the

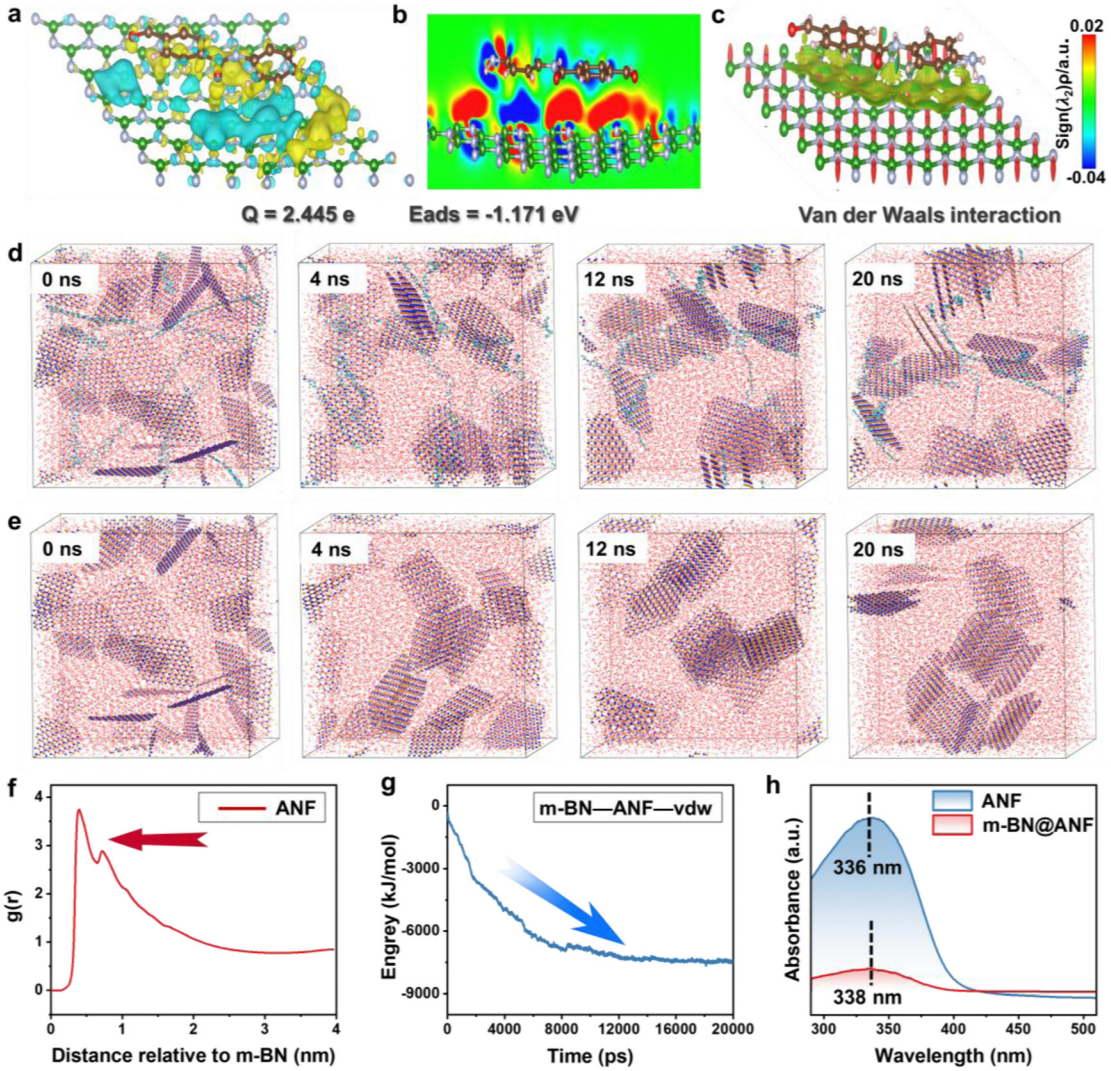

Fig. 3 The stabilization mechanism of the m-BN@ANF ink. (a) Charge density difference in m-BN@ANF. (b) ELF map for m-BN@ANF. (c) RDG of m-BN@ANF. (d) Snapshots of assembly of m-BN with ANF in water simulated using the GROMACS package. (e) Snapshots of m-BN in water simulated using the GROMACS package. (f) RDF of ANF at different relative distances to m-BN. (g) van der Waals forces between m-BN and ANF. (h) UV-vis spectra of m-BN@ANF ink and ANF dispersion.

π–π interaction between the phenyl group of ANF and the basal plane of the m-BN.[46–48]

Preparation and characterization of m-BN@ANF papers

In view of its good dispersibility, the m-BN@ANF ink could yield high-quality m-BN@ANF papers by various film-forming methods, such as blade coating, casting, and vacuum filtration techniques. This proves its excellent film-forming ability and good universality to the film-forming methods (Fig. S10, ESI†). Here, we mainly utilize the slurry properties to achieve large-scale preparation of m-BN@ANF papers *via* a blade coating process (Fig. 4a). Interestingly, the obtained m-BN@ANF papers could be cut, bent, twisted, and folded without breakage, indicating their good tailorability and high mechanical flexibility (Fig. 4b). The cross-sectional morphology is investigated to gain insights into the internal structures of the m-BN@ANF papers. It is found that the m-BN@ANF papers exhibit a densely stacked and laminar structure, in which the large-sized m-BN closely overlap with each other and are highly oriented along the in-plane direction. In addition, the ANF tightly adheres to the surface of the m-BN, resembling a highly compact "brick–mortar" structure (Fig. 4c–f and Fig. S11, ESI†).[49,50] Furthermore, the orientation of the m-BN@ANF papers was characterized using 2D wide-angle X-ray scattering (WAXD) measurements. The outermost halo corresponds to the (002) plane of m-BN (Fig. 4g), while the sharp peak observed on the azimuthal integral curve in the (002) scattering plane was attributed to the highly ordered arrangement of m-BN in the direction parallel to the in-plane direction, with an orientation of 0.75 (Fig. 4h).

As shown in Fig. 4i of the Fourier transform infrared spectroscopy (FTIR), the in-plane bending vibration of m-BN at 1374 cm^{-1} and the out-of-plane bending stretching of m-BN at 818 cm^{-1} exhibit resonance with the aryl ring

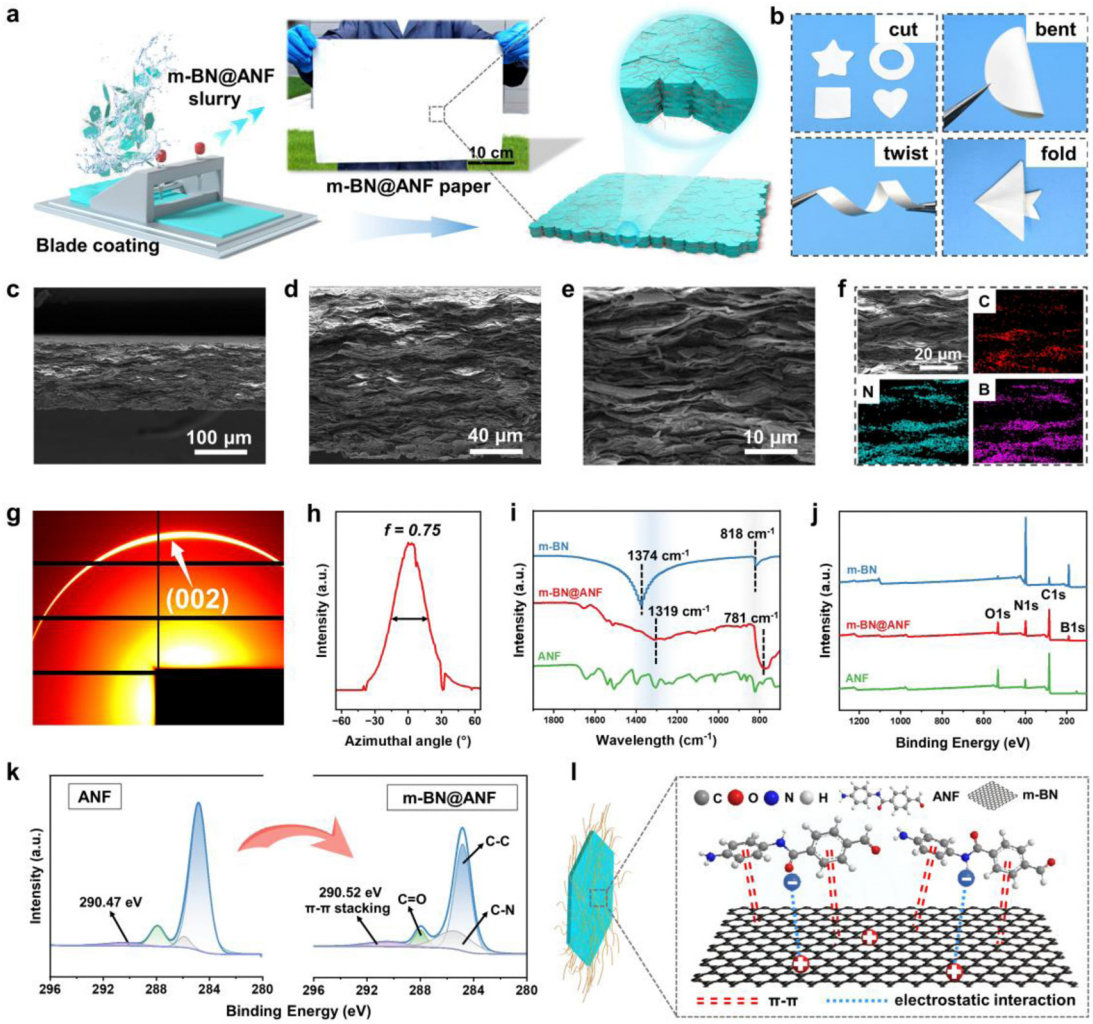

Fig. 4 Preparation and characterization of m-BN@ANF papers. (a) Schematic illustration of the fabrication process of the m-BN@ANF papers *via* a blade coating method. (b) Digital photographs of m-BN@ANF papers in the cut, bent, twisted, and folded state. (c)–(e) SEM images of the m-BN@ANF papers. (f) SEM and the corresponding C, N, and B elemental EDS mapping images of the m-BN@ANF papers. (g) WAXD patterns of the m-BN@ANF papers in the cross-section direction. (h) Azimuthal integral curve in the (002) scattering plane for the m-BN@ANF papers. (i) FTIR spectrum of the ANF papers, m-BN, and the m-BN@ANF papers. (j) XPS patterns of the ANF papers, m-BN, and the m-BN@ANF papers. (k) C1s spectra of the ANF and m-BN@ANF papers. (l) Schematic diagram of the interaction between m-BN and ANF in the m-BN@ANF papers.

vibration of the ANF at 1399 cm^{-1} and 825 cm^{-1}, respectively. The resonance causes the overlapping of the characteristic peaks of m-BN and ANF, resulting in the formation of a single peak, which shifts toward a lower wavenumber. This phenomenon indicates that strong π–π interaction exists between the m-BN and ANF in the insulating papers.[44] The XPS spectrum shows that the C1s spectrum of ANF paper exhibits a π–π stacking characteristic feature peak at 290.47 eV, which corresponds to the binding energy of π-electrons in the aromatic ring of ANF. Compared to ANF, the π–π stacking peak in the C1s spectrum of m-BN@ANF paper moves to 290.52 eV, confirming the formation of strong π–π interaction between m-BN and the aromatic rings of ANF. In addition, the π–π stacking peak moves towards higher energy, indicating that the π-electron cloud density of ANF decreases and electrons transfer from ANF to m-BN (Fig. 4j and k).[51–53] These results confirm the formation of strong π–π interaction between the m-BN and ANF (Fig. 4l).

Electrical insulation properties of the m-BN@ANF papers

The E_b represents the capacity of the electrical insulating materials to withstand voltage, which directly reflects their insulation level.[1,15] To analyze the E_b of the m-BN@ANF papers, a two-parameter Weibull distribution function is applied to fit the failure statistics (Fig. 5a). With increasing m-BN content, the E_b of the m-BN@ANF papers exhibits a trend of rapid increase and then decrease. Notably, the m-BN90 paper achieves the highest E_b value of 233.5 kV mm^{-1}, which is 73.6% higher than that of the ANF papers (Fig. 5b and Fig. S12, ESI†). The superior E_b value of the m-BN@ANF papers is attributed to the high orientation of the wide bandgap m-BN perpendicular to the electric field direction, which promotes

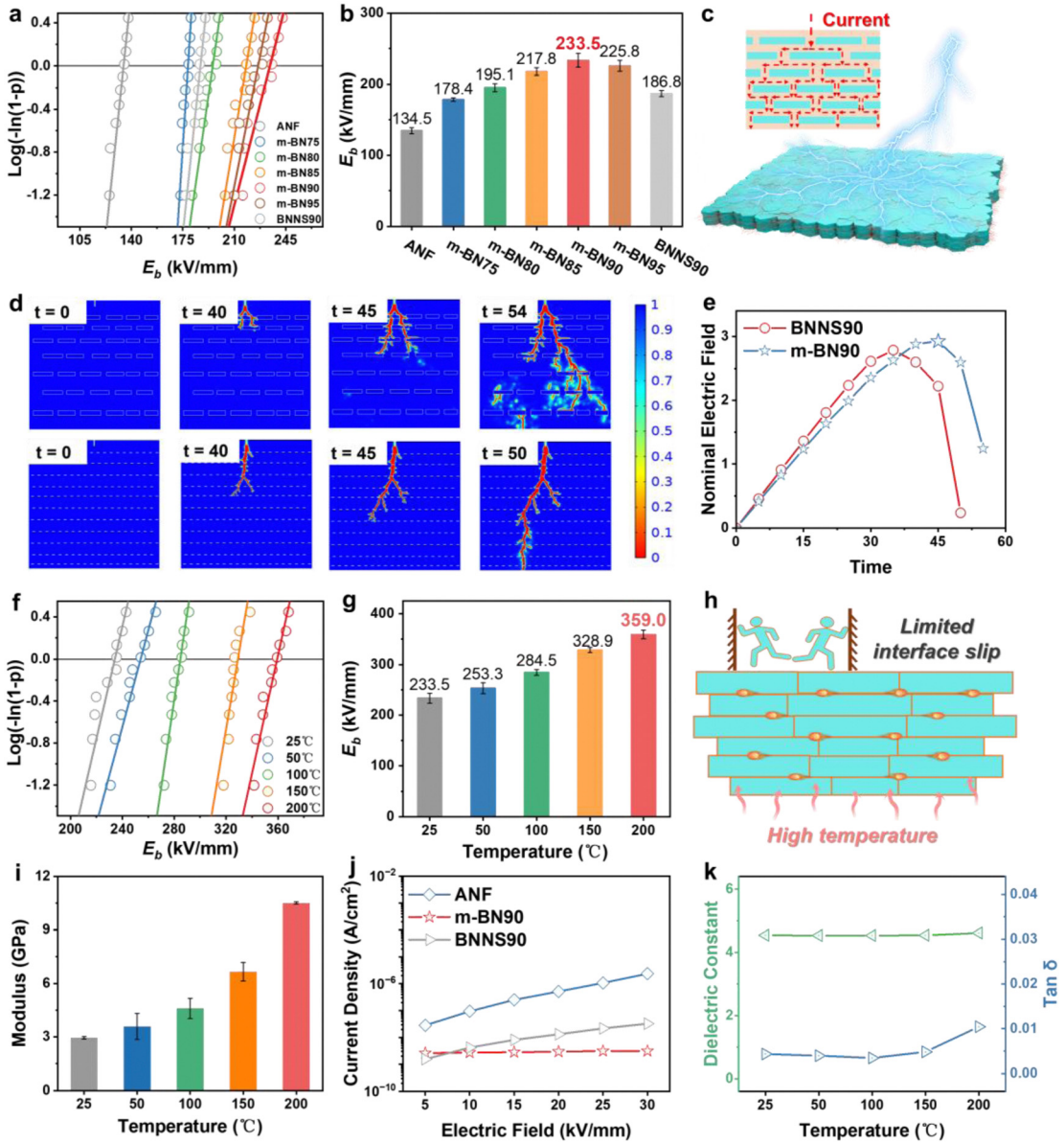

Fig. 5 Electrical insulation properties of the m-BN@ANF papers. (a) Weibull distribution and (b) E_b values of the ANF, m-BN@ANF, and BNNS90 papers. (c) Schematic diagram of electric tree breakdown for the m-BN@ANF papers. (d) Finite element simulation and (e) nominal electric field intensity distribution of the m-BN90 and BNNS90 models. (f) Weibull distributions and (g) E_b values of the m-BN90 paper at different temperatures. (h) Electric breakdown mechanism at high temperatures. (i) Modulus of the m-BN90 paper at different temperatures. (j) Leakage current densities of the ANF, m-BN90, and BNNS90 papers. (k) Dielectric constants and loss factors of the m-BN90 paper at a frequency of 10^4 Hz and different temperatures.

charge dissipation in the transverse direction and hinders the transport of free electrons (Fig. 5c).[1] Finite element simulation is employed to analyze the breakdown process, and the results indicate that the m-BN90 paper exhibits a more tortuous breakdown path of the electrical tree compared to the BNNS90 paper. After the insulating papers were completely broken down, the nominal field intensity of the m-BN90 paper was higher than that of the BNNS90 paper, these results strongly prove the positive contribution of the large lateral size of m-BN in the enhancement of E_b (Fig. 5d, e and Fig. S13, ESI†).

The rapid development of modern industries such as electric vehicles, underground oil/gas exploration, and aerospace systems, puts high demands on the ability of insulating papers to withstand voltage at high temperatures.[8,54] Indeed, it is well known that the E_b values of conventional polymer papers sharply decrease at high temperatures.[9] In sharp contrast, our m-BN@ANF papers exhibit marked enhancements in E_b as the temperature increases from 25 °C to 200 °C (Fig. 5f and g). In particular, the E_b value of the m-BN90 paper reaches 359.0 kV mm^{-1} at a high temperature of 200 °C, which is 53.7% higher than the E_b value at ambient temperature (Fig. S14, ESI†). This result is closely related to the increase in Young's modulus due to the restricted interfacial slip of m-BN at high temperatures (Fig. 5h, i and Fig. S15, ESI†).[13,14] The

highest electromechanical breakdown strength (E_{EM}) can be analyzed by the following equation:

$$E_{EM} = 0.606\sqrt{\frac{Y}{\varepsilon_0 \varepsilon_r}} \quad (2)$$

where Y is the Young's modulus, ε_0 and ε_r are the permittivity of vacuum and the relative permittivity, respectively.[2] The higher Young's modulus suggests a lower possibility of electromechanical breakdown for the m-BN90 paper, resulting in a higher E_b value at high temperatures. It was also found that the m-BN@ANF papers exhibit extremely high electrical resistance, meeting the evaluation criteria for electrical insulation ($>1 \times 10^9$ Ω cm) (Fig. S16, ESI†). In addition, the leakage current density of the m-BN90 paper retains a level of 3.1×10^{-9} A cm^{-2} at 30 kV mm^{-1}, which is significantly lower than that of BNNS90 paper and the pure ANF paper (Fig. 5j). Moreover, upon increasing the temperature, the dielectric constant and loss factor of the m-BN90 paper remain relatively stable at a frequency of 10^4 Hz, which are maintained in the range of 4.5–4.6 and 0.004–0.010, respectively (Fig. 5k and Fig. S17, ESI†).[14] These results verify the reliable electrical insulation properties of the m-BN@ANF papers.

To highlight the advantages of our m-BN@ANF papers, the E_b values are thoroughly compared with previously reported insulating papers and some commercial insulating papers, as shown in Table S2 (ESI†).[8,12–14,55–60] We find that the E_b value of our m-BN@ANF papers is superior to most of these insulating papers over a wide range of temperatures, which can be attributed to the large lateral size of the wide bandgap m-BN, intrinsic outstanding thermal stability of m-BN and ANF, and the tightly stacked lamellar structure of m-BN@ANF papers. These superior electrical insulation properties make the m-BN@ANF papers ideal insulating materials for applications in high-temperature circumstances.

Thermal and mechanical properties of the m-BN@ANF papers

For electrical insulation applications at elevated temperatures, high TC is also desirable for insulating papers.[5] Thermal conductivity tests reveal that the TC of the m-BN@ANF papers tends to increase significantly and then slightly decrease with increasing m-BN content. The maximum value of TC reaches 26.4 W m^{-1} K^{-1} at 90 wt% m-BN content, which is improved by 905% and 27% compared with the pure ANF paper and the BNNS90 paper (Fig. 6a and Fig. S18, ESI†).[23] The outstanding TC of our m-BN@ANF papers is attributed to the intrinsic high thermal conductivity of both m-BN and ANF, and the larger interfacial contact area and fewer number of interfacial boundaries induced by the large lateral size of m-BN in the composite papers, which together promote the phonon transport efficiency (Fig. 6b).[30] Finite element simulation is used to verify the heat transfer mechanism of the composite papers (Fig. S19, ESI†), and the corresponding temperature distributions are shown in Fig. 6c. Obviously, the heat mainly transports along the boron nitride (BN) from the bottom (heat source) to the top part, and the temperature gradient is mainly caused by phonon scattering at the BN overlapped interface. At the same location, the temperature of the m-BN90 paper is higher than that of the BNNS90 paper, confirming the superiority of m-BN as a thermal conductive building block in the composite papers (Fig. 6d).[22]

To highlight the superiority of our work, the TC of our m-BN@ANF papers is compared with other reported BN based papers prepared by various methods, including electrostatic spinning, vacuum filtration, and the sol–gel-film method (Fig. 6e).[6,15,24,25,61–70] The results demonstrate that the TC value of our m-BN90 paper prepared by a facile blade coating method surpasses that of most of the BN based thermally conductive papers reported in the literature. Furthermore, to increase the objectivity of the TC data for m-BN@ANF papers, the TC enhancement efficiency of BN was evaluated using specific TC (defined as the ratio of the increase in TC to the BN content). The results show that the m-BN90 paper exhibits an excellent specific TC value of 0.265 W m^{-1} K^{-1} wt%$^{-1}$, outperforming most values previously reported in the literature (Table S3 and Fig. S20, ESI†). Although some of the specific TC reported in the literature are higher than that of our work, their TC value is still at a lower level, which is due to the lower BN addition in those works. These results indicate that our work has successfully achieved superior TC and high TC enhancement efficiency at high m-BN content.

Insulating papers are inevitably subjected to mechanical damage during practical applications, outstanding mechanical properties are of great significance for insulating papers to ensure the safety and reliability of electrical equipment. The m-BN90 paper exhibits superior mechanical properties, with a tensile strength of 30.0 MPa (Fig. 6f), which was mainly attributed to the strong π–π interactions between the ANF chains and the m-BN, and relatively few interfacial defects in the composites. Moreover, the small sized m-BN90 paper could easily lift a weight of 500 g without breaking, demonstrating the robust mechanical performance of m-BN@ANF papers (Fig. S21, ESI†). Thermal stability and flame retardancy of insulating papers are of great value in practical applications. Thermogravimetric analysis (TGA) is carried out to investigate the thermal stability of the papers (Fig. 6g).[71,72] The initial thermal decomposition temperature of m-BN90 paper is 486 °C, which is 38 °C higher than that of the ANF paper. The improvement of thermal stability can be attributed to the introduction of m-BN, which possesses an ultra-high temperature resistance over 800 °C. The vertical burning tests, the limited oxygen index (LOI) tests, and the micro calorimetric (MCC) tests were used to systematically evaluate the flame retardancy of insulating papers. The vertical burning tests reveal that m-BN90 paper self-extinguishes immediately after being exposed to the flame for 10 s, with no molten drops, and therefore pass the VTM-0 rating (Fig. 6h and Fig. S22, ESI†).[73] The LOI value of m-BN90 paper reaches 60%, demonstrating excellent flame retardancy of the m-BN@ANF composite (Fig. S23, ESI†).[74] Furthermore, Fig. 6i and Fig. S24 (ESI†) show some important flame-retardancy parameters such as heat release rate (HRR), peak heat release rate (PHRR), total heat release rate (THR), heat release capacity (HRC), and peak

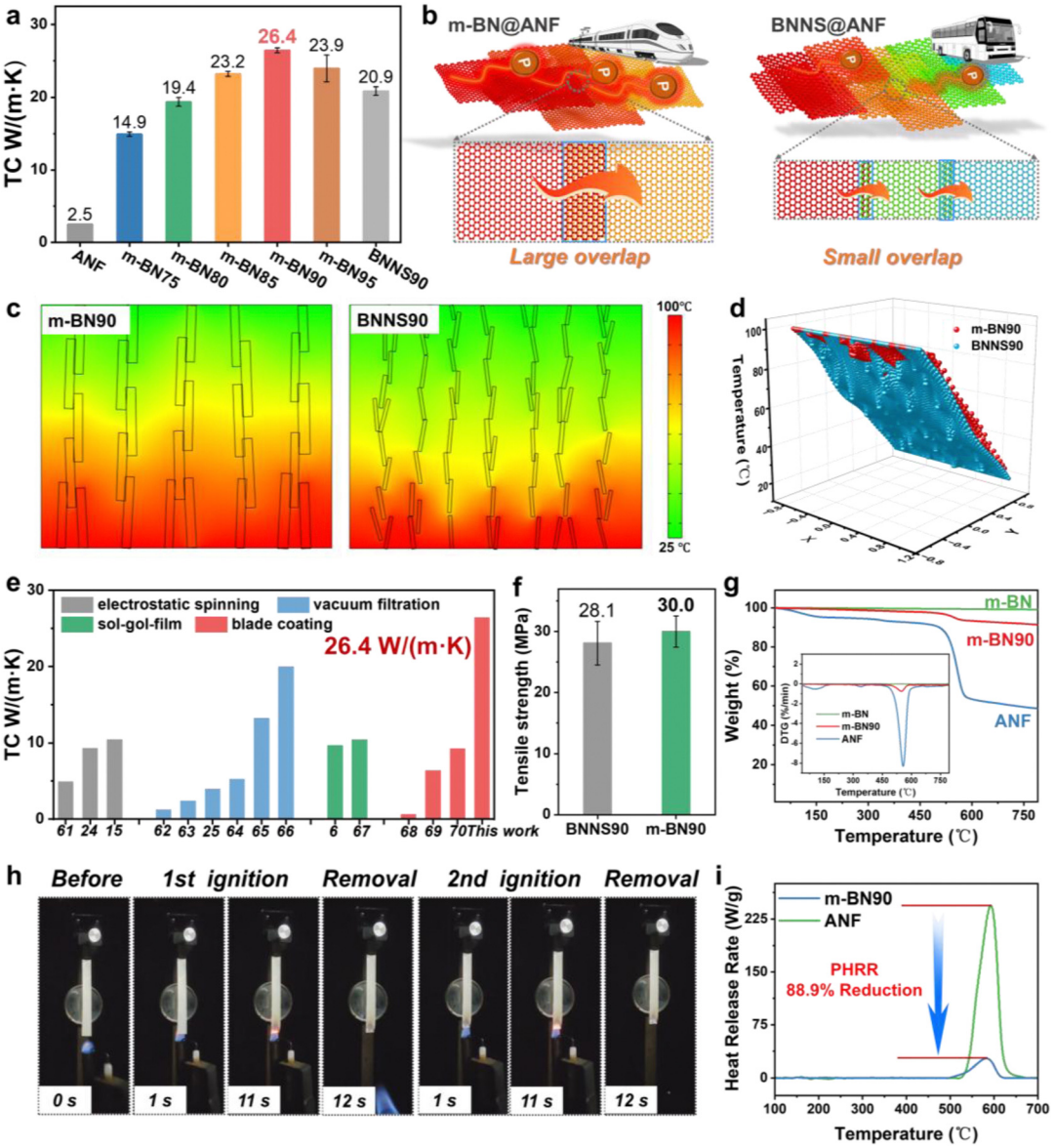

Fig. 6 Thermal and mechanical properties of the m-BN@ANF papers. (a) In-plane TC of insulating papers with different filler contents. (b) Schematic of thermal conductivity mechanism of m-BN@ANF papers. (c) Finite element simulation of heat transfer in the composite papers. (d) Temperatures recorded at different points in the composite papers. (e) Comparison of the TC values of the prepared m-BN90 paper with those of previously reported BN based papers. (f) Tensile strengths of the m-BN90 paper and the BNNS90 paper. (g) TGA and DTG curves of the ANF paper, m-BN, and the m-BN90 paper. (h) Snapshots of vertical burning tests for the m-BN90 paper. (i) HRR *versus* temperature curves of m-BN90 and ANF papers.

heat release temperature (T_{PHRR}), and the specific data are summarized in Table S4 (ESI†). The m-BN90 paper exhibits a PHRR value of 27.3 W g^{-1}, a T_{PHRR} value of 582.4 °C, and a THR value of 1.5 kJ g^{-1}. Compared to the ANF with excellent flame-retardancy properties, the m-BN@ANF papers show more excellent flame-retardancy performance.[75] All these results indicate that the m-BN@ANF insulating paper is an ideal flame-retardant material, thanks to the intrinsically excellent flame-retardant properties of m-BN and ANF (Fig. S25, ESI†). Overall, the m-BN@ANF papers integrate with ultra-high breakdown strength, superior thermal conductivity and good thermal stability, which make it a robust and powerful option for future electrical insulation materials that need to be used in high-temperature circumstances.

Application of the m-BN@ANF papers

To visualize the in-plane heat transfer capability of the m-BN@ANF papers, the m-BN90 paper and the ANF paper were placed vertically on a heating plate, and the surface temperature distributions of the papers were recorded using an infrared camera (Fig. 7a and b). The corresponding temperature curves presented in Fig. 7c show that the m-BN90 paper exhibits a higher temperature than the ANF paper at the same distance from the heat source, which reveals the superior heat transfer

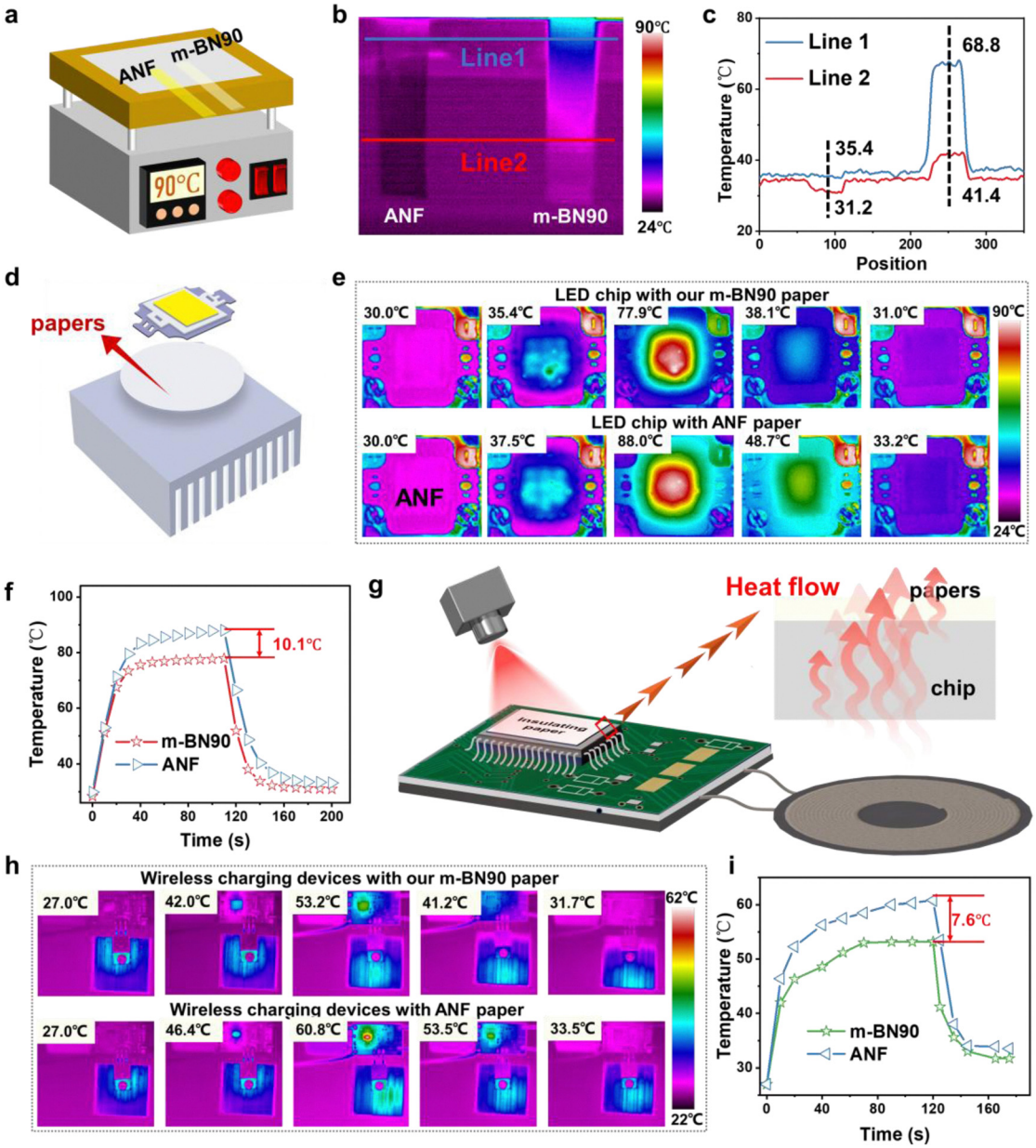

Fig. 7 Application of the m-BN@ANF papers. (a) Schematic diagram of thermal conductivity test apparatus for the m-BN90 paper and ANF paper. (b) Infrared thermal images of the m-BN90 and the ANF papers. (c) Temperature curves of the m-BN90 and the ANF papers. (d) Schematic diagram, (e) infrared thermal images, and (f) temperature evolution curves for the m-BN90 and ANF papers as heat spreaders between an aluminum heat sink and an LED chip. (g) Schematic diagram, (h) infrared thermal images, and (i) temperature evolution curves for the wireless charging device chips with m-BN90 and ANF papers.

capacity of the m-BN@ANF papers. A typical electronic element was employed to further assess the heat dissipation behaviors of the m-BN@ANF papers. The m-BN90 paper and the ANF paper were placed between the high-power light emitting diode (LED) chip (10 W) and an aluminum heat sink for heat transfer (Fig. 7d and Fig. S26, ESI†). Upon operation of the LED chip, the surface temperature of the LED chip using m-BN90 paper stabilizes faster (50 s) and has a lower stabilization temperature (77.9 °C) compared to the use of ANF paper. Similarly, after turning off the power, the m-BN90 paper requires a shorter time to reach a lower stabilization temperature, demonstrating the good heat transfer capability of the m-BN@ANF papers (Fig. 7e and f).

Further, the insulating paper was applied to a wireless charging device to verify its thermal management capability in electronic devices (Fig. S27, ESI†). Typically, insulating paper was placed on the surface of the chip of the wireless charging device, as shown in Fig. 7g. The results show that our m-BN@ANF exhibits a prominent cooling effect compared to the ANF. For example, after 120 s of operation of the wireless charging device, the chip temperature reached 53.2 °C with the m-BN@ANF paper, which is 7.6 °C lower than that of the

chip with ANF (Fig. 7h and i). These results emphasize the importance of our research, that is, through the assembly of m-BN, we prepared insulating papers with excellent insulation performance and efficient thermal management ability, which show great prospects in the high temperature insulation application field of modern electronic equipment.

Conclusion

We report a universal and scalable one-step assembly strategy to realize the preparation of high-temperature-resistant insulating papers by coupling m-BN with fibrous ANF. The jellyfish-like structure of ANF plays a crucial role in achieving a stable dispersion for the m-BN@ANF ink, which facilitates the large-scale preparation of nacre-like high-performance insulating papers. The prepared m-BN@ANF papers achieve an ultra-high breakdown strength of 359.0 kV mm^{-1} even at a high temperature of 200 °C. In addition, the insulating papers have a superior thermal conductivity of 26.4 W m^{-1} K^{-1}, excellent thermostability with an initial decomposition temperature of 486 °C, and outstanding flame retardancy with a VTM-0 rating. These advantages render m-BN@ANF papers ideal insulating materials for electrical equipment. Therefore, this study provides a novel approach for developing high-performance insulating papers for electrical engineering equipment that operate under high-temperature conditions.

Experimental

Materials

Poly-*p*-phenylene terephthalamide (PPTA, Kevlar 49) fibers, with an average diameter of approximately 15 μm and a density of 1.44 g cm^{-3}, were purchased from DuPont. Micron-BN sheets (m-BN) with lateral sizes of approximately 10 μm were provided by the Key Laboratory of Micro and Nano-scale Boron Nitride Materials, Hebei Province, China. Potassium hydroxide (KOH) and dimethyl sulfoxide (DMSO) were provided by Chengdu Kelong Chemical Reagent. Deionized water was obtained from the laboratory water purification system.

Fabrication of the m-BN@ANF papers

The weight method was employed to control the mass fractions of components in the composite papers. The masses of m-BN and ANF required for the preparation of various m-BN@ANF papers were calculated and measured. For instance, 9 g of m-BN and 1 g of ANF were weighed to prepare the m-BN90 paper. The ANF dispersion was prepared by the deprotonation of the PPTA fibers in a strong alkaline system. More specifically, 1.2 g of PPTA and 1.8 g of KOH were added to 160 mL of DMSO and 6.4 mL of deionized water, and then mechanically stirred for 72 h at room temperature to obtain a red ANF dispersion. Subsequently, m-BN was added into the ANF dispersion under mechanical agitation and ultrasonication for 15 min, and the obtained mixture was poured into deionized water and allowed to stir for 10 min to promote protonation and generate m-BN@ANF floccules. These floccules were then washed several times with deionized water by vacuum filtration to obtain the m-BN@ANF filter cake. The filter cake was dispersed into a certain amount of deionized water and homogenized with a high-speed homogenizer at 10 000 rpm for 10 min to obtain the m-BN@ANF ink. After, the m-BN@ANF ink was alternately filtered through a polytetrafluoroethylene membrane (0.22 μm in pore size) to fabricate the m-BN@ANF papers. Finally, each composite paper was mechanically compressed at 35.0 MPa and at room temperature for 20 min to promote densification. For comparison, the ANF papers and BNNS@ANF papers were prepared using the same approach. For simplicity, the m-BN@ANF papers using 75, 80, 85, 90, and 95 wt% m-BN content were denoted as m-BN75, m-BN80, m-BN85, m-BN90, and m-BN95, respectively, while the BNNS@ANF paper prepared using a 90 wt% BNNS content was denoted as BNNS90.

Characterization

The microstructures of the PPTA fibers, m-BN, and the m-BN@ANF papers were observed using a field emission scanning electron microscope (FESEM, Inspect-F, FEI, Finland) at an acceleration voltage of 5 kV. The elemental distribution of the m-BN@ANF papers was analyzed using an Ultim Max energy-dispersive spectrometer (EDS). The morphologies of ANF dispersion and m-BN@ANF ink were captured using a transmission electron microscope (TEM) instrument (FEI, Tecnai G2 F20) at an acceleration voltage of 200 kV. The orientation of the m-BN90 paper was measured by wide-angle X-ray diffraction (WAXD, Bruker Nanostar) at beamline 16B of the Shanghai Synchrotron Radiation Facility (Shanghai, China). The specimens were further analyzed using X-ray diffraction (XRD, DX-1000 diffractometer), Fourier transform infrared spectroscopy (FTIR, Nicolet 6700, Thermal Scientific), UV-vis spectrometer (UV-vis, Lambda750s), and X-ray photoelectron spectroscopy (XPS, Thermo Kalpha). The stability of the m-BN@ANF ink and the m-BN dispersion was monitored using multiple light scattering instruments (Turbiscan Lab, Formulaction, France). The zeta potential of the ANF and m-BN@ANF ink were determined using dynamic light scattering particle size analysis (Zetasizer Nano ZS90, UK). The viscosity and modulus of the m-BN90 slurry were measured using a rotational rheometer (MCR302, Anton Paar, Austrian) equipped with a parallel plate (25 mm diameter). The breakdown strength of the specimens was characterized using a high voltage tester (19057-20, Chroma) with a DC voltage. Resistivity was measured using a DC resistance tester (TH2684). The leakage current density of the prepared papers was measured using a Radiant Technologies Precision Premier II (Radiant Tech.) equipped with a high voltage amplifier (TREK MODEL 609B, 10 kV). The dielectric constant and loss factor of nanopapers at different temperatures (25–200 °C) were measured using an inductance, capacitance, and resistance meter (Agilent Tech., HP 4294A) within the frequency range from 1 kHz to 1 MHz with a 0.5 V alternating current signal, and the temperature was controlled using a link (TMS 94) controller system. The thermal

conductivity (λ) of the specimens was calculated according to the following equation $\lambda = \alpha \times \rho \times Cp$, where α, ρ and Cp represent the thermal diffusivity, density, and specific heat capacity of the specimens, respectively. The thermal diffusivity of the specimens was measured using an LFA 467 HyperFlash (NETZSCH, Germany) at 25 °C. The density of the specimens was calculated by a weighing method. Thermogravimetric analysis (TGA) of the samples was performed on a NETZSCH TG209 F1 thermal analyzer with a heating rate of 10 °C min^{-1} under a nitrogen atmosphere. Vertical combustion tests were conducted according to ISO 9773 in Tech-GBT2408, the sample was cut to 120 mm × 13 mm and the number of valid tests was 5. The limiting oxygen index tests were conducted based on ISO 4589-2 in TTech-GBT2406-1, the samples were cut to 80 mm × 10 mm and the number of valid tests was 5. The micro calorimetric test was performed on a DEATAK MCC-3 calorimeter according to ASTM D7309-2007. Infrared (IR) images were recorded using an RNO thermal infrared imager to evaluate the heat conduction in the prepared specimens. The Young's modulus of the samples at different temperatures was determined using a dynamic thermomechanical analyzer (TMA, Q850, TA Instruments, USA). The stress–strain curves of the m-BN90 and BNNS90 papers were measured using an Instron 5967 series instrument at a loading rate of 1.0 mm min^{-1}.

Author contributions

Meng-Xin Liu: data curation, formal analysis, and writing – original draft. Rui-Yu Ma: formal analysis and methodology. Zhi-Xing Wang: formal analysis and data curation. Zhuo-Yang Li: formal analysis and software. Gui-Lin Song: formal analysis and software. Jie Lin: formal analysis and software. Xin-Yuan Li: formal analysis and investigation. Ling Xu: conceptualization and writing – review & editing. Ding-Xiang Yan: writing – review & editing. Li-Chuan Jia: conceptualization, funding acquisition, writing – review & editing. Zhong-Ming Li: conceptualization, writing – review & editing.

Data availability

The authors confirm that the data supporting the findings of this study are available within the article and its ESI.†

Conflicts of interest

There are no conflicts to declare.

Acknowledgements

This work was supported by the National Natural Science Foundation of China (grant no. 52103043) and the Key Laboratory of Engineering Dielectrics and Its Application (the Harbin University of Science and Technology), Ministry of Education (grant no. KFM202306).

References

1 T. Wang, J. Mao, B. Zhang, G. Zhang and Z. Dang, *Nat. Rev. Electr. Eng.*, 2024, **1**, 516–528.
2 Q. Feng, S. Zhong, J. Pei, Y. Zhao, D. Zhang, D. Liu, Y. Zhang and Z. Dang, *Chem. Rev.*, 2022, **122**, 3820–3878.
3 T. Zhang, L. Yang, C. Zhang, Y. Feng, J. Wang, Z. Shen, Q. Chen, Q. Lei and Q. Chi, *Mater. Horiz.*, 2022, **9**, 1273–1282.
4 X. Zhou, P. Min, Y. Liu, M. Jin, Z. Yu and H. Zhang, *Science*, 2024, **385**, 1205–1210.
5 Y. Zhou, Z. Zhang, Q. Tang, X. Ma and X. Hou, *Mater. Horiz.*, 2024, **11**, 4348–4358.
6 L. Tang, K. Ruan, X. Liu, Y. Tang, Y. Zhang and J. Gu, *Nano-Micro Lett.*, 2023, **16**, 38.
7 L. Su, X. Ma, J. Zhou, X. Liu, F. Du and C. Teng, *Nano Res.*, 2022, **15**, 8648–8655.
8 W. Sun, Z. Han, X. Yue, H. Zhang, K. Yang, Z. Liu, D. Li, Y. Zhao, Z. Ling, H. Yang, Q. Guan and S. Yu, *Adv. Mater.*, 2023, **35**, 2300241.
9 R. Wang, Y. Zhu, J. Fu, M. Yang, Z. Ran, J. Li, M. Li, J. Hu, J. He and Q. Li, *Nat. Commun.*, 2023, **14**, 2406.
10 Y. Liu, W. Zou, N. Zhao and J. Xu, *Nat. Commun.*, 2023, **14**, 5342.
11 B. Zhang, J. Liu, M. Ren, C. Wu, T. J. Moran, S. Zeng, S. E. Chavez, Z. Hou, Z. Li, A. M. LaChance, T. R. Jow, B. D. Huey, Y. Cao and L. Sun, *Adv. Mater.*, 2021, **33**, 2101374.
12 F. Zeng, X. Chen, G. Xiao, H. Li, S. Xia and J. Wang, *ACS Nano*, 2020, **14**, 611–619.
13 X. Pan, G. Yu, H. Gao, Z. Wang, Z. Bao, X. Li and S. Yu, *Adv. Mater.*, 2022, **34**, 2206855.
14 X. Pan, Z. Bao, W. Xu, H. Gao, B. Wu, Y. Zhu, G. Yu, J. Chen, S. Zhang, L. Li, H. Wu, X. Li and S. Yu, *Adv. Funct. Mater.*, 2023, **33**, 2210901.
15 J. Chen, X. Huang, B. Sun and P. Jiang, *ACS Nano*, 2019, **13**, 337–345.
16 L. Zhao, Y. Liao, L. Jia, Z. Wang, X. Huang, W. Ning, Z. Zhang and J. Ren, *Polymers*, 2021, **13**, 2028.
17 L. Zhao, C. Wei, Z. Li, W. Wei, L. Jia, X. Huang, W. Ning, Z. Wang and J. Ren, *Mater. Des.*, 2021, **210**, 110124.
18 M. Li, M. Wang, X. Hou, Z. Zhan, H. Wang, H. Fu, C. Lin, L. Fu, N. Jiang and J. Yu, *Composites, Part B*, 2020, **184**, 107746.
19 W. Liang, Q. Wu, R. Han, L. Li and M. Nie, *Langmuir*, 2024, **40**, 25978–25987.
20 P. Du, Z. Wang, J. Ren, L. Zhao, S. Jia and L. Jia, *ACS Appl. Electron. Mater.*, 2022, **4**, 4622–4631.
21 M. Li, Y. Zhu and C. Teng, *Compos. Commun.*, 2020, **21**, 100370.
22 J. Ren, G. Jiang, Z. Wang, Q. Qing, F. Teng, Z. Jia, G. Wu and S. Jia, *Adv. Compos. Hybrid Mater.*, 2024, **7**, 5.
23 L. Zhao, L. Wang, Y. Jin, J. Ren, Z. Wang and L. Jia, *Composites, Part B*, 2022, **229**, 109454.
24 T. Wang, G. Zhang, B. Zhang, S. Liu, D. Li and C. Liu, *ACS Appl. Nano Mater.*, 2021, **4**, 4153–4161.

25 T. Ma, Y. Zhao, K. Ruan, X. Liu, J. Zhang, Y. Guo, X. Yang, J. Kong and J. Gu, *ACS Appl. Mater. Interfaces*, 2020, **12**, 1677–1686.
26 C. Yao, G. Leahu, M. Holicky, S. Liu, B. Fenech-Salerno, M. C. Lai, M. C. Larciprete, C. Ducati, G. Divitini, R. L. Voti, C. Sibilia and F. Torrisi, *Adv. Funct. Mater.*, 2024, **34**, 2405235.
27 H. He, W. Peng, J. Liu, X. Y. Chan, S. Liu, L. Lu and H. Le Ferrand, *Adv. Mater.*, 2022, **34**, 2205120.
28 J. Zhu, F. Li, Y. Hou, H. Li, D. Xu, J. Tan, J. Du, S. Wang, Z. Liu, H. Wu, F. Wang, Y. Su and H. Cheng, *Nat. Mater.*, 2024, **23**, 604–611.
29 S. Roy, X. Zhang, A. B. Puthirath, A. Meiyazhagan, S. Bhattacharyya, M. M. Rahman, G. Babu, S. Susarla, S. K. Saju, M. K. Tran, L. M. Sassi, M. A. S. R. Saadi, J. Lai, O. Sahin, S. M. Sajadi, B. Dharmarajan, D. Salpekar, N. Chakingal, A. Baburaj, X. Shuai, A. Adumbumkulath, K. A. Miller, J. M. Gayle, A. Ajnsztajn, T. Prasankumar, V. V. J. Harikrishnan, V. Ojha, H. Kannan, A. Z. Khater, Z. Zhu, S. A. Iyengar, P. A. da, S. Autreto, E. F. Oliveira, G. Gao, A. G. Birdwell, M. R. Neupane, T. G. Ivanov, J. Taha-Tijerina, R. M. Yadav, S. Arepalli, R. Vajtai and P. M. Ajayan, *Adv. Mater.*, 2021, **33**, 2101589.
30 K. Zhang, Y. Feng, F. Wang, Z. Yang and J. Wang, *J. Mater. Chem. C*, 2017, **5**, 11992.
31 G. Han, B. Zhou, Z. Li, Y. Feng, C. Liu and C. Shen, *Mater. Horiz.*, 2023, **10**, 3051–3060.
32 W. Qian, H. Fu, Y. Sun, Z. Wang, H. Wu, Z. Kou, B. Li, D. He and C. Nan, *Adv. Mater.*, 2022, **34**, 2206101.
33 T. Liu, F. Wang, Q. Wu, T. Chen and P. Sun, *Mater. Horiz.*, 2021, **8**, 3096–3104.
34 D. Thapa, S. B. Sharma, D. Alfè, D. Kilin and S. Kilina, *Mater. Horiz.*, 2024, **11**, 3613–3622.
35 Z. Zhao, Z. Wang, Y. Yu and Y. Hu, *Small*, 2023, **19**, 2302489.
36 M. Zheng, Z. Fang, W. Xue, T. Yan, H. Huang and C. Zhong, *Adv. Funct. Mater.*, 2024, 2422135.
37 I. V. Yudanov, A. Genest, S. Schauermann, H. Freund and N. Rösch, *Nano Lett.*, 2012, **12**, 2134–2139.
38 J. Zhang, X. Liu, Y. Ji, X. Liu, D. Su, Z. Zhuang, Y. Chang, C. Pao, Q. Shao, Z. Hu and X. Huang, *Nat. Commun.*, 2023, **14**, 1761.
39 W. Ren, J. Liang, M. Huang, W. Qian, M. Zhao, F. Qiao, L. Cui, Z. Zhang, J. Wang, C. Zhou, Z. Wang, Q. An and D. He, *Chem. Eng. J.*, 2024, **498**, 155811.
40 L. Jia, Z. Wang, L. Wang, J. Zeng, P. Du, Y. Yue, L. Zhao and S. Jia, *Mater. Horiz.*, 2023, **10**, 5656–5665.
41 X. Xie, Y. Jiang, X. Yao, J. Zhang, Z. Zhang, T. Huang, R. Li, Y. Chen, S. Li and Y. Lan, *Nat. Commun.*, 2024, **15**, 5017.
42 B. Zheng, F. L. Oliveira, R. Neumann Barros Ferreira, M. Steiner, H. Hamann, G. X. Gu and B. Luan, *ACS Nano*, 2023, **17**, 5579–5587.
43 J. L. Suter, R. C. Sinclair and P. V. Coveney, *Adv. Mater.*, 2020, **32**, 2003213.
44 K. Wu, J. Wang, D. Liu, C. Lei, D. Liu, W. Lei and Q. Fu, *Adv. Mater.*, 2020, **32**, 1906939.
45 X. Li, T. Xu and Y. Gong, *Phys. Chem. Chem. Phys.*, 2024, **26**, 12044–12052.
46 X. Han, H. Kong, T. Chen, J. Gao, Y. Zhao, Y. Sang and G. Hu, *Nanomaterials*, 2021, **11**, 2158.
47 J. Fan, Z. Shi, L. Zhang, J. Wang and J. Yin, *Nanoscale*, 2012, **4**, 7046–7055.
48 D. Ji, Z. Zhang, J. Sun, W. Cao, Z. Wang, X. Wang, T. Cao, J. Han and J. Zhu, *ACS Appl. Mater. Interfaces*, 2024, **16**, 25304–25316.
49 Y. Wang, Y. Bao and W. Meng, *ACS Nano*, 2024, **18**, 23655–23671.
50 J. Wang, X. Ma, J. Zhou, F. Du and C. Teng, *ACS Nano*, 2022, **16**, 6700–6711.
51 D. Zhang, W. Song, L. Lv, C. Gao, F. Gao, H. Guo, R. Diao, W. Dai, J. Niu, X. Chen, J. Wei, M. Terrones and Y. Wang, *Carbon*, 2023, **214**, 118315.
52 Y. Cheng, H. Cheng, J. Gao, Y. Xue, G. Han, B. Zhou, C. Liu, Y. Feng and C. Shen, *Small*, 2024, 2409408.
53 A. Zhang, Z. Wang, Z. Fang, J. Li and T. Liu, *Angew. Chem.*, 2024, **136**, e202412777.
54 J. Chen, Y. Zhou, X. Huang, C. Yu, D. Han, A. Wang, Y. Zhu, K. Shi, Q. Kang, P. Li, P. Jiang, X. Qian, H. Bao, S. Li, G. Wu, X. Zhu and Q. Wang, *Nature*, 2023, **615**, 62–66.
55 N. Li, Z. Lu, X. Ji, D. Ning, N. Yan and Songfeng E, *ACS Appl. Nano Mater.*, 2024, **7**, 9925–9933.
56 M. Li, Y. Zhu and C. Teng, *Compos. Commun.*, 2020, **21**, 100370.
57 M. Li, M. Wang, X. Hou, Z. Zhan, H. Wang, H. Fu, C. Lin, L. Fu, N. Jiang and J. Yu, *Composites, Part B*, 2020, **184**, 107746.
58 Y. Min, J. Yu, P. Xu, P. Li, S. Luo, B. Chu and S. Yu, *ACS Appl. Mater. Interfaces*, 2022, **14**, 51265–51274.
59 J. Wang, H. Guo, S. Zeng, J. Du, Q. Zhang and K. Wang, *Chem. Eng. J.*, 2024, **492**, 152237.
60 Q. Feng, Y. Zhang, D. Liu, Y. Song, L. Huang and Z. Dang, *Mater. Today Energy*, 2022, **29**, 101132.
61 R. Wu, X. Song, Y. Ji, H. Wu, S. Guo and J. Qiu, *Compos. Sci. Technol.*, 2024, **251**, 110573.
62 R. Tian, X. Jia, M. Lan, J. Yang, S. Wang, Y. Li, D. Shao, L. Feng and H. Song, *Chem. Eng. J.*, 2022, **446**, 137255.
63 M. M. Rahman, A. B. Puthirath, A. Adumbumkulath, T. Tsafack, H. Robatjazi, M. Barnes, Z. Wang, S. Kommandur, S. Susarla, S. M. Sajadi, D. Salpekar, F. Yuan, G. Babu, K. Nomoto, S. Islam, R. Verduzco, S. K. Yee, H. G. Xing and P. M. Ajayan, *Adv. Funct. Mater.*, 2019, **29**, 1900056.
64 S. Chen, R. Xu, J. Liu, X. Zou, L. Qiu, F. Kang, B. Liu and H. Cheng, *Adv. Mater.*, 2019, **31**, 1804810.
65 Z. Wang, W. Liu, Y. Liu, Y. Ren, Y. Li, L. Zhou, J. Xu, J. Lei and Z. Li, *Composites, Part B*, 2020, **180**, 107569.
66 Y. Shang, Y. Ji, J. Dong, G. Yang, X. Zhang, F. Su, Y. Feng and C. Liu, *Compos. Sci. Technol.*, 2021, **214**, 108974.
67 H. Tu, K. Xie, X. Lin, R. Zhang, F. Chen, Q. Fu, B. Duan and L. Zhang, *J. Mater. Chem. A*, 2021, **9**, 10304–10315.
68 M. Se Chang, S. Hwang, S. Jeong, J. Won Jeong, B. Park, S. Yang, C. Rae Park and Y. Kwon, *Chem. Eng. J.*, 2023, **475**, 146496.
69 O. H. Kwon, T. Ha, D. Kim, B. G. Kim, Y. S. Kim, T. J. Shin, W. Koh, H. S. Lim and Y. Yoo, *ACS Appl. Mater. Interfaces*, 2018, **10**, 34625–34633.

70 C. Teng, L. Su, J. Chen and J. Wang, *Composites, Part A*, 2019, **124**, 105498.
71 Y. Li, M. Liu, C. Li, K. Cui, L. Li and L. Jia, *Composites, Part B*, 2025, **296**, 112269.
72 X. Li, J. Lin, J. Wu, M. Liu, P. Du, L. Xu, D. Yan, L. Jia and Z. Li, *Adv. Funct. Mater.*, 2025, 2420839.
73 Y. Liu, W. Zou, N. Zhao and J. Xu, *Nat. Commun.*, 2023, **14**, 5342.
74 Z. Wang, W. Wu and X. Gong, *Mater. Horiz.*, 2025, DOI: **10.1039/D4MH01684J**.
75 J. Liu, Y. Xiao, Y. Wang, Y. Wuliu, X. Zhu, L. Zhang and X. Liu, *Mater. Horiz.*, 2024, **11**, 5274–5284.

